PHYSICAL REVIEW B VOLUME 40, NUMBER 15 15 NOVEMBER 1989-II

Time-of-flight scattering and recoiling spectrometry.
I. Structure of the W(211) surface

O. Grizzi,* M. Shi, H. Bu, and J. W. Rabalais
Department of Chemistry, University of Houston, Houston, Texas 77204-5641

P. Hochmann
College of Sciences and Mathematics, The University of Texas at San Antonio, San Antonio, Texas 78285

(Received 14 April 1989; revised manuscript received 13 July 1989)

The technique of time-of-flight scattering and recoiling spectrometry (TOF-SARS) with detection of both neutrals and ions is presented and the scattering technique is applied to structural analysis of the clean W(211) surface. The recoiling technique is applied to structural analysis of oxygen and hydrogen on this surface in the two papers (II and III) immediately following this one (I). This series of three papers emphasizes the ability to obtain direct "real-space" information on the relative positions of atoms in the surface region based on simple classical concepts. In this first paper, both backscattering (BS) and forward-scattering (FS) from a pulsed 4-keV Ar^+ primary-ion beam are monitored as a function of polar beam incident angle α, polar beam exit angle β, surface azimuthal angle δ, and scattering angle θ for clean W(211). Plots of BS intensities in (α,δ) space provide scattering structural contour maps and three-dimensional scattering structural plots of the clean W(211) surface. Measurements of BS intensities at $\theta = 163°$ as a function of α along crystal azimuths with known interatomic spacings in the first layer are used to obtain experimental points on the shadow cones. These experimental points allow calibration of the screening constants in the interatomic potentials used in trajectory simulations and calculations of the shadow cones as well as calibration of the surface vibrational amplitudes used for simulation of the BS flux distributions. The experimental data and calibrated computations are applied to determination of surface relaxation, both changes in first- to second-layer spacing and first- and second-layer registry, for the (211) structure. The results show that the first- to second-layer spacing is contracted by 0.12 Å (9.3%) and that there is a lateral shift along the $[1\bar{1}\bar{1}]$ direction such that the layer registry is shifted by 0.10 Å (3.6%). The calibrated interatomic potentials are used to simulate blocking cones for FS measurements in the range $0° < \theta < 55°$. The sensitivity of TOF-SARS to the details of atomic structure, its ability to probe the first layer as well as subsurface layers, focusing and channeling effects that enhance BS and FS along certain azimuths, and the ability to extract surface structural information with only simple calculations are discussed.

I. INTRODUCTION

Low-energy (< 10 keV) ion-scattering spectrometry, having had its beginning[1] more than 20 years ago, is presently one of the most actively developing surface-science techniques due to important advances that have been recently realized.[2] Among these are the use of (i) impact-collision ion-scattering spectrometry[3–9] (ICISS) in which the scattering angle θ is close to 180°, thus simplifying the scattering geometry and allowing experimental determination of the shadow cone radii; (ii) alkali-metal primary ions[10–16] which have low neutralization probabilities, leading to higher scattered-ion fluxes in ICISS; (iii) time-of-flight (TOF) techniques[17–22] with detection of both neutrals and ions in order to enhance sensitivity; (iv) scattered-ion fractions[5,6,23] to probe the spatial distributions of electrons; and (v) the use of recoiling[24] to determine the structure of light adsorbates on surfaces. The reason for the intense interact in this technique is that it provides direct "real-space" information on the relative positions of atoms in the surface region based on simple classical concepts. This makes it complementary to diffraction techniques, such as low-energy electron diffraction (LEED),[25] for which the elucidation of reconstructed and relaxed surface structures and the determination of adsorbate-site positions and bond lengths from reciprocal-space patterns are often formidable and, in some cases, ambiguous tasks.

This paper (I) is the first member of a series of three papers. This series describes and demonstrates the technique of time-of-flight scattering and recoiling spectrometry (TOF-SARS) for determination of surface structure and adsorbate site positions and coordinates relative to the substrate lattice. The abbreviations and symbols used in this series are listed in Table I. The technique uses TOF methods for analysis of both scattered (S) and recoiled neutrals (N) and ions (I) simultaneously and applies classical-trajectory simulation, shadow cone, and ion flux distribution calculations for modeling the collision processes. The method can be summarized as follows. In the keV range, ions scatter from atomic cores (nuclei plus core electrons). Analysis of the *total scattered and recoiled neutral plus ion flux* as a function of incident angle provides direct information on *surface atom-*

TABLE I. List of abbreviations and symbols. This table presents all of the abbreviations and symbols used in this paper and papers II (Ref. 37) and III (Ref. 38). Not all of these are used in this first paper.

A	horizontal distance within the first-layer plane from a first-layer atom to a position above a second-layer atom
BS	backscattering event
BZ	Biersack-Ziegler potential function
C	scaling factor for potential-function screening length
DR	direct-recoil event
E_0	energy of primary ion
F	scattered-ion fraction
FS	forward-scattering event
FWHM	full width at half maximum
I	ion
I(BS)	backscattering intensity
I(DR)	direct-recoil intensity
IFCM	ion-fraction contour map
IFP	ion-fraction plot
I(FS)	forward-scattering intensity
$I(R)$	recoiling intensity
$I(S)$	scattering intensity
I(SR)	surface recoil intensity
L	distance behind shadowing atom along ion beam direction
M	Molière potential function
M_1	mass of primary ion
M_2	mass of target atom
ML	monolayer
MS	multiple scattering
N	neutrals
N_E	counts in constant energy increments
N_t	counts in constant time increments
$R(L)$	radius of shadow cone at distance L behind shadowing atom
RSCM	recoiling structural contour map
RSP	recoiling structural plot
S	scattering event
SARS	scattering and recoiling spectrometry
SBC	single–binary-collision event
SF	scaling factor for spectral intensities
SR	surface recoil event
SS	quasisingle scattering event
SSCM	scattering structural contour map
SSP	scattering structural plot
TOF	time of flight
X(DR)	direct recoil event for target atom X
$X(R)$	recoil event for target atom X
X(SR)	surface recoil event for target atom X
Z	vibrational amplitude of surface atoms
b	distance from first layer plane to edge of shadow cone taken along the normal to the surface and passing through A
c	correction due to finite p size resulting from the use of $\theta < 180°$
d	vertical distance from second-layer atom to first-layer plane
p	impact parameter
r	distance from first-layer W atom to adsorbate atom in the [211] plane and along the direction of alignment of the W and adsorbate atom
t_{DR}	TOF of particle recoiled in a single binary collision (direct recoil)
t_{SS}	TOF of particle scattered in a single binary collision [single scattering (SS)]
x	$[01\bar{1}]$ coordinate or horizontal distance of adsorbate atom from $[1\bar{1}\bar{1}]$ rows
z	[211] coordinate or vertical distance of adsorbate atom above first-layer plane
Θ	adsorbate coverage in monolayers

TABLE I. (*Continued*).

α	polar beam incident angle
α_c	critical incident angle
$\alpha^i_{c,\mathrm{sh}}$	ith critical incident angle in a I(BS) or I(DR) vs α scan; determined by shadowing cones
$\alpha_{c,\mathrm{bl}}$	critical incident angle at highest α position in a I(DR) vs α scan; determined by blocking cones
β	polar beam exit angle
β_c	critical exit angle
δ	surface azimuthal angle
l	distance from target to detector
ϕ	recoiling angle
θ	scattering angle

ic core positions that is independent of electron exchange (neutralization) effects. Analysis of the *angular distributions of scattered-ion fractions* $F=[(N+I)-N]/(N+I)$ provides direct information on *electronic transition probabilities* between the ion and surface atoms. Both the structural and electron transfer probability measurements can be made in a single experiment by alternately collecting $N+I$ and N.

There are two basic physical phenomena which govern these processes. First, *interatomic interactions,* described by the laws of classical mechanics, control the scattering and recoiling trajectories of keV ions. Hence, collecting $N+I$ spectra provides data which are only dependent on structural effects and independent of electron neutralization effects. The interatomic potentials which describe these interactions are well known,[26,27] allowing calculation of scattering and recoiling trajectories from which structural information can be directly derived by comparison with experimental results. Second, *electronic transition probabilities* control the ion-surface neutralization process; collecting F data gives direct information on these electronic transitions.[28–31]

The information content of the $(N+I)$ data is as follows. Since the scattering and recoiling trajectories are determined by the impact parameters and atomic structure of the surface, resolution of structure on an atomic scale can be obtained by collecting data as a function of the scattering angle θ, recoil angle ϕ, incident angle α, ejection angle β, and azimuthal angle δ (see Fig. 1 for the definition of these angles). Plots of scattering $I(S)$ [or recoiling $I(R)$] intensity in (α,δ) space provide scattering (or recoiling) structural contour maps (SSCM) [or (RSCM)] and three-dimensional scattering (or recoiling) structural plots (SSP) [or (RSP)]. These plots summarize the experimental structural data into characteristic structural features ("fingerprints") of clean surfaces and adsorbates on those surfaces which are specific to the energy and type of projectile ion used.

The W(211) surface along with hydrogen and oxygen chemisorption are studied in this series. This is an excellent system for exemplifying the structural capabilities of TOF-SARS because the W(211)surface has an open, corrugated structure and, moreover, it is important to quantitate the relaxation of the clean surface[32] and to resolve the controversy[33–36] concerning the adsorbate-site positions. The (211) surface of bcc W, shown in Fig. 1, consists of parallel close-packed rows of atoms separated by wide channels. The open structure and low spatial symmetry of such a high index surface can be expected to differ from the simple bulk-truncated surface by relaxation both perpendicular (different interlayer spacings) and parallel (change in layer registry) to the surface. Davis and Wang[32] have used LEED to study this relaxation of the clean W(211) surface; their results suggest that the first-atomic layer is relaxed 0.09 Å parallel to, and 0.16 Å perpendicular to, the surface. This provides a test case for the structural ability of TOF-SARS.

This paper (hereafter referred to as I) presents details of the application of TOF-SARS to structural analysis of a clean W(211) surface using Ar^+ ions in the backscattering (BS) mode with $\theta=163°$ and forward-scattering (FS) mode with $0° \leq \theta \leq 55°$. The following other papers of this series [henceforth II (Ref. 37) and III (Ref. 38)] present the structural analysis of oxygen and hydrogen, respectively, on W(211) using a combination of both BS and recoil measurements.

The paper is organized as follows. The experimental techniques employed are described in Sec. II. The experimental results are presented in Sec. III in the form of example TOF spectra, α and β scans, scattering structural contour map and scattering structural plot, and qualitative interpretations. Section IV describes the computer simulations, shadowing and blocking cones, and BS flux distribution calculation techniques, calibration, and computational results. Relaxation of the (211) surface is calculated in Sec. V. These results are discussed in Sec. VI and the findings are summarized in Sec. VII.

II. EXPERIMENTAL METHODS

A. TOF-SARS instrument

The measurements were carried out in a custom-designed UHV spectrometer system (base pressure 1×10^{-10} Torr), shown schematically in Fig. 2, that will be described in detail elsewhere.[39] The system was designed for (i) TOF measurements of scattered,[28] recoiled,[40,41] and sputtered[42] particles (neutrals and/or ions) from a surface over a continuous angular range as stimulated by a pulsed ion beam, (ii) kinetic energy measurements of scattered, recoiled, and sputtered ions, (iii) x-ray and uv photoelectron spectroscopy (XPS and UPS),

(iv) electron- and ion-induced Auger-electron spectroscopy (AES), and (v) low-energy electron diffraction. This series of papers focuses on the use of the TOF scattering and recoiling portion of the system. Ions are created in the source by electron-impact ionization of gases and then accelerated up to 5 keV. The pulsed ion beam line (*A* in Fig. 2) is similar to one that has been described previously,[23] producing pulse widths of ~50 ns with average current densities of 0.05–5.0 nA/mm^2. Typical current densities used in these experiments were ~0.1 nA in a 1-mm-diam spot size. The pressure in the scattering chamber rose to $\sim 1\times 10^{-8}$ Torr during measurements due to Ar gas from the beam line. A channel electron multiplier (CEM) detector, which is sensitive to both ions and fast neutrals, was mounted on a long tube which is connected to a precision rotary-motion feedthrough (*E* in Fig. 2), allowing rotation of the detector in vacuum over a scattering angular range of $0^\circ \le \theta \le 165^\circ$ and providing a flight path of 98.4 cm. The timing electronics and pulsing sequence are similar to those that have been published previously.[23] Data are collected into a multichannel pulse-height analyzer and stored in a minicomputer.

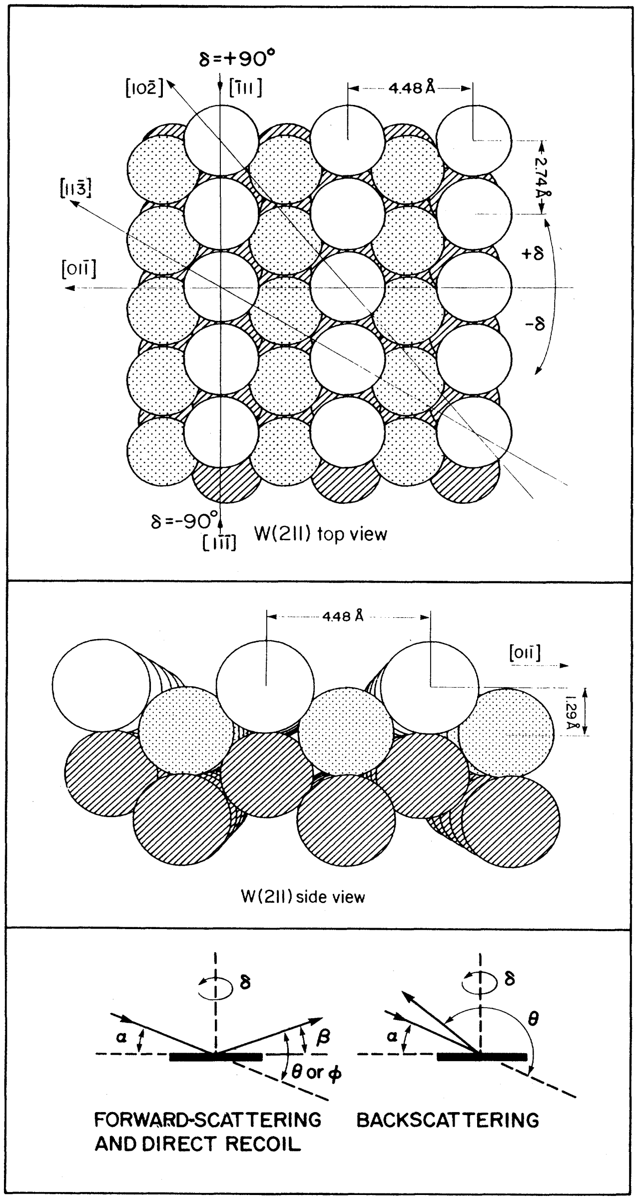

FIG. 1. Structure of the bulk-truncated W(211) surface along with the definition of angles used herein. Open circles, first-layer atoms; dotted circles, second-layer atoms; dashed circles, third- and fourth-layer atoms.

B. Sample cleaning and spectral acquisition

The W(211) crystal was in the form of a disk with diameter 1 cm and thickness 1 mm and was oriented to <0.5°. It was polished with successively finer grits of alumina down to 0.05 μm and its orientation was determined from the x-ray diffraction pattern. The crystal was mounted on a precision manipulator that allowed both polar incident and azimuthal rotations, translations along three orthogonal axes, and adjustment of the sample tilt angle with respect to the incident ion beam. The angular notation used herein is defined in Fig. 1. The crystal was cleaned inside the chamber by annealing (by electron bombardment from the back of the crystal). Several days of temperature cycling from room temperature up to 2300 K were required to produce a clean surface after exposure to atmosphere. Temperature was measured by means of a portable infrared thermometer. Surface cleanliness was monitored by both TOF-SARS and AES. Due to the high sensitivity[43] of TOF-SARS to light atoms [i.e., detectability of <0.01 monolayer (ML) of surface contamination], the "clean" surface condition was taken to be the case of absence of recoiled hydrogen, carbon, and oxygen signals in the TOF spectra. No carbon or oxygen contamination was detectable by AES for this surface condition. Cleanliness with respect to the TOF-SARS test proved to be much more difficult to achieve than with the AES test due to the high sensitivity of the former. The clean crystal produced a sharp (1×1) LEED pattern as observed previously.[33,34] The beam incident angle α and the scattering angle θ were aligned by means of a laser beam. The azimuthal angle δ was aligned by monitoring surface semichanneling[26] of the incident beam through the $[1\,\bar{1}\,\bar{1}]$ troughs in the FS mode and by aligning the (1×1) LEED pattern. The resulting accuracy was ±1° for α and θ and ±1.5° for δ, although the reproducibility of these angular positions was <±0.5°.

BS and FS TOF spectra were collected by counting for periods of typically 20 sec. Scans of scattering intensity versus polar incident angle α were obtained by fixing the scattering angle θ and surface azimuthal angle δ and rotating the crystal along an axis contained by the surface plane and perpendicular to the scattering plane so as to vary α. The angle α was varied from 0° (ion beam parallel to crystal surface) up to 90° in 1°, 2°, or 3° increments and the TOF spectra were stored at each point for later analysis. An increment of 1° was used in regions with sharp structure and larger steps were used in relatively flat regions. The crystal was reannealed following each α scan in order to avoid contamination and surface damage. Such α scans were made along different azimuths for $-96° \leq \delta \leq +96°$ in increments of 6°, where $\delta = 0°$ corresponds to the $[01\bar{1}]$ azimuth, $\delta = 90°$ corresponds to the $[\bar{1}11]$ azimuth, and $\delta = -90°$ corresponds to the $[1\bar{1}\bar{1}]$ azimuth. Since the measurements were made on different days, it was difficult to establish the exact same conditions; therefore it was necessary to calibrate the intensities along different azimuths. This was accomplished by choosing several specific angles α and measuring the BS and FS intensities as a function of δ in order to obtain calibration factors for normalizing the previous scans.

C. General procedure for structural determination

The general procedure for structural determination by TOF-SARS is as follows. (i) I(BS) versus α scans are measured along those azimuths δ for which the lattice spacings are accurately known. (ii) These data are used to calibrate the screening constant of the interatomic potential in shadow cone calculations in order to obtain highly accurate cone dimensions. (iii) I(BS) versus α scans are made along different azimuths, particularly high-symmetry azimuths and those in the region where the first- and second-layer lattice atoms are believed to be aligned. (iv) These data, along with the calibrated cones, are used to determine the first- and second-layer registry and vertical spacing. Rather than follow this straightforward four-step procedure, this paper provides considerable detail on spectral interpretation, spectral sensitivity to lattice features, computational procedures, ion trajectories, and symmetry features of the scattering data. The objective of this is to determine the rich information content of the scattering data.

III. EXPERIMENTAL RESULTS AND INTERPRETATIONS

This section presents the experimental results in the form of example TOF spectra and polar incident α, azimuthal δ, and ejection β angular scans along with their qualitative interpretations.

A. TOF spectra

Structural analyses require the intensities of the BS peaks from the TOF spectra. Typical BS and FS TOF spectra for 4-keV Ar^+ scattering from a clean W(211) surface are shown in Fig. 3. The sharp peaks correspond to Ar (quasi)single scattering (SS) from W atoms. The TOF for scattering of an incident ion of mass M_1 and energy E_0 from a target atom of mass M_2 into an angle θ from a binary collision is given by

$$t_{SS} = l(M_1+M_2)/(2M_1E_0)^{1/2} \times \{\cos\theta \pm [(M_2/M_1)^2 - \sin^2\theta]^{1/2}\} , \tag{1}$$

where l is the distance from the target to detector. Equation (1) applies to only cases for $M_2/M_1 > 1$. The absence of H, C, and O recoil signals in the FS spectrum is a clear indication of the cleanliness of the surface. This FS spectrum was collected within the region of highest sensitivity for detection of these contaminants, i.e., $8° \leq \alpha \leq 15°$ and $35° \leq \phi \leq 45°$, as will be shown in II (Ref. 37) and III.[38] The TOF spectra were transformed to energy spectra as described elsewhere.[23] The scattering peaks are very close to the E corresponding to Ar scat-

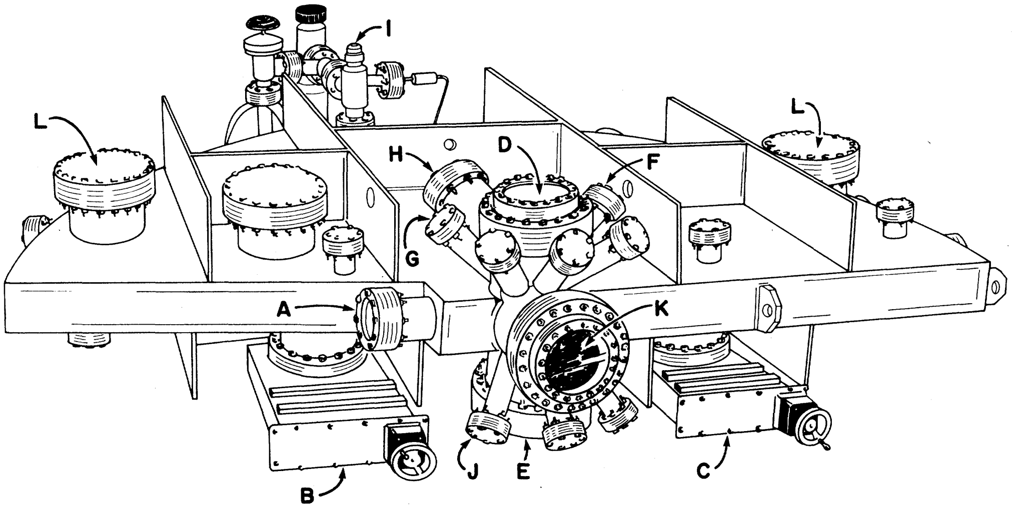

FIG. 2. Spectrometer system designed for TOF analysis of neutrals and ions and ESA analysis of ions that are scattered and recoiled along with conventional AES, XPS, UPS, and LEED analysis. A, pulsed ion beam; B, turbomolecular pump; C, ion pump; D, sample manipulator; E, detector precision rotary motion feedthrough; F, x-ray source; G, electron gun; H, 180° electrostatic hemispherical analyzer; I, sorption pumps; J, sputter ion gun; K, viewport or reverse view LEED optics; L, titanium sublimation pump.

tered by a single binary collision (SBC) from W. Both the FS and BS spectra exhibit energy-loss tails on the low-E sides of the scattering peaks.

At the 4-keV projectile energy employed, the measured width (0.3-μsec FWHM) and position of the maximum for the BS peak were independent (within 0.1 μsec) of the α and δ orientations of the sample. This confirms that the major contribution to the BS peak intensity originates from SS collisions. Projectiles BS through multiple-scattering (MS) collisions have TOF distributions that are broader than those observed here and are dependent on the α and δ directions. As an example of a possible MS sequence, consider the case of an Ar^+ projectile scattered at a total angle $\theta=163°$ through two consecutive binary collisions of $\theta=81.5°$ each, with the two W atoms separated by 2.74 Å (interatomic distance along the $[1\bar{1}\bar{1}]$ rows). The calculated cross section and TOF for such an event are 20 times smaller and 0.6 μsec shorter, respectively, than the corresponding values for the SS sequence at 163°. These and similar MS sequences are responsible for shoulders observed along certain α and δ directions on the BS peaks. The heights of these shoulders were always $<30\%$ of the heights at the SS position of the BS peaks, allowing determination of the true SS intensities to an accuracy of better than 20%; the reproducibility of these intensities was within 10%. As a representative measure of I(BS), the counts were integrated over a TOF window of 0.4 μsec centered over the SS peak maximum following background subtraction. The background was taken as the average number of counts/channel on the short TOF side (flat region near 4 μsec) of the BS peak multiplied by the number of channels in the TOF window. The dependence of I(BS) on α for different δ is described in Sec. III B.

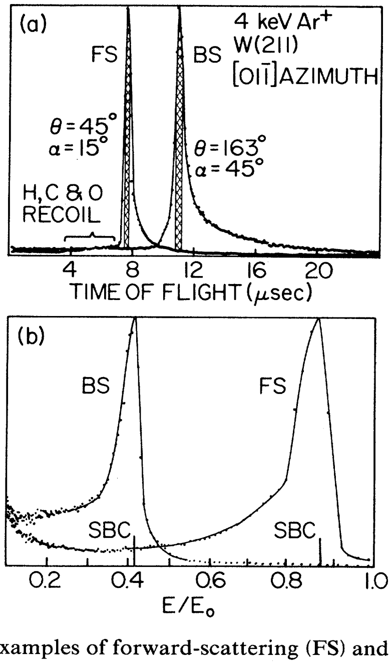

FIG. 3. Examples of forward-scattering (FS) and backscattering (BS) TOF (a) and energy (b) spectra for 4-keV Ar^+ scattering from a clean W(211) surface. The beam direction was along the $[01\bar{1}]$ azimuth, the FS spectrum was collected at $\theta=45°$, $\alpha=15°$, and the BS spectrum was collected at $\theta=163°$, $\alpha=45°$. Both spectra are normalized to the same total intensity. The positions corresponding to single binary collisions (SBC) of Ar with W are indicated. The areas measured as Ar BS intensity, I(BS), and Ar FS intensity, I(FS), are shown hatched. The BS window contained ten channels and the FS window contained six channels. The spectral region for impurity H, C, and O recoils is indicated.

At FS angles, the SS and certain MS sequences have comparable scattering cross sections and the TOF differences between them can be very small; this makes the analysis of I(FS) more difficult than that of I(BS). In this case, the intensities were obtained by integrating the counts over a TOF window of only 0.2 μsec centered over the FS peak maximum.

B. Polar incident α scans

Collecting I(BS) data as a function of α allows one to probe the ability of the incident ions to make a direct hit, i.e., near zero impact parameter p, on W atoms in specific surface and subsurface layers. Example plots of experimental BS Ar intensities at $\theta=163°$ versus incident angle α are shown in Fig. 4 for several different crystal azimuths δ. Single-, double-, and triple-peaked structures, depending on the crystal orientation, can be observed in such plots. The common features of these plots are (i) the low BS intensities observed at grazing incidence and (ii) the good agreement of the position of the sharp initial slope and height of the first low α peak for scans along equivalent azimuths, i.e., $\pm\delta$, of opposite sign. The

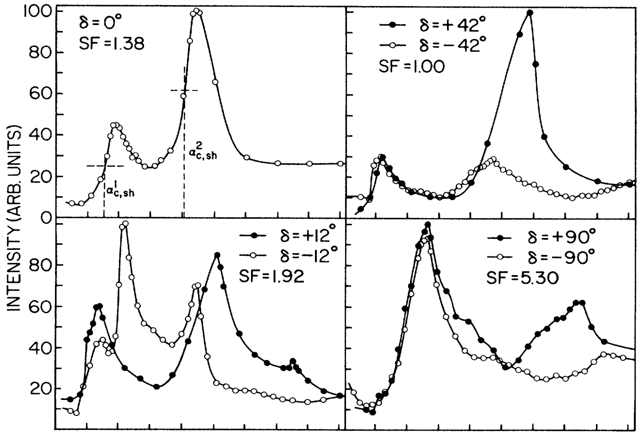

FIG. 4. Examples of experimental backscattered (BS) Ar neutral plus ion ($N+I$) intensities as a function of incident angle α at $\theta=163°$ for several different crystal azimuths δ. The scaling factors (SF) indicate the numbers by which the spectral points were multiplied in order to place the peak of maximum intensity at 100. Lines are used to connect the data points in order to guide the eye. The critical incident angles $\alpha^i_{c,\mathrm{sh}}$ are indicated for the $[01\bar{1}]$ azimuth.

reason for (i) is that at grazing incidence each surface atom is shadowed from the incoming ion beam by its neighboring atoms. Therefore, for an ideal atomically flat surface, only FS can occur at very small α. BS can only occur when the top-layer atoms begin to move out of the shadow cones cast by their neighbors and head-on ($p \approx 0$) collisions become possible. The steep rises and well-defined maxima observed in the I(BS) versus α scans of Fig. 4 are due to focusing of the ion trajectories by the atomic potentials. The ion trajectories are bent by the target atom potential such that an excluded volume, i.e., a *shadow cone,* in the shape of a paraboloid is formed behind the target atom. The deflected trajectories are concentrated at the edges of the shadow cone. When α is such that the edge of the shadow cone passes through the center of an adjacent atom, this *focusing effect* causes sharp rises in I(BS). The thermal vibrations of the atoms around their equilibrium positions and imperfections in the surface structure broaden the ideally vertical step rise in the onset of I(BS).

The BS intensity at grazing incidence and the specific onset and sharpness of the rise in I(BS) are sensitive to imperfections in the surface structure. This provides a check of the adequacy of the annealing process prior to each scan. An example of this is shown in Fig. 5 for the case of a well-annealed surface and the same surface after bombardment with a dose of 3×10^{14} ions/cm^2 of 4-keV Ar$^+$. The difference curve plotted in Fig. 5 shows that I(BS) is higher at grazing incidence and lower in the region of the first focusing peak for the bombarded surface; this is the expected behavior for surfaces with missing atoms, steps, or rough structures. This effect was found to be completely reversible, i.e., smooth annealed or rough bombarded surfaces could be generated repeatedly. The area under this difference curve at low α is related[39] to the degree of surface damage or roughness.

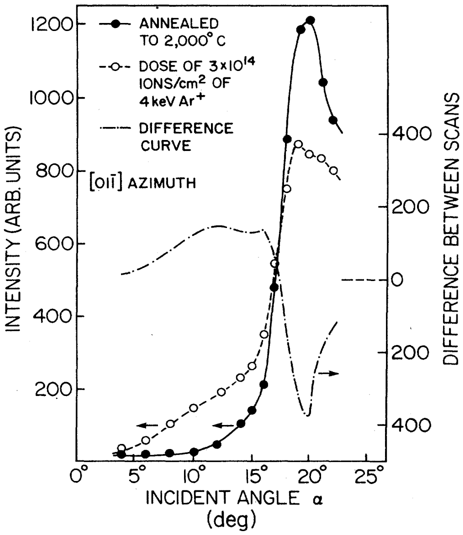

FIG. 5. Plots of backscattering intensity I(BS) vs incident beam angle α at $\theta=163°$, $\delta=0°$ for 4-keV Ar$^+$ on a smooth annealed surface and the same bombarded (dose of 3×10^{14} ions/cm^2 of 4-keV Ar$^+$) surface. The difference curve representing $I(\mathrm{BS})_{\mathrm{rough}}-I(\mathrm{BS})_{\mathrm{smooth}}$ is also shown.

The α positions of the sharp rises in I(BS) were taken as one-half of the peak height minus the background. These critical values of α result from shadowing by neighboring atoms and are labeled $\alpha^i_{c,\mathrm{sh}}$ in the figures; the index i labels the $\alpha_{c,\mathrm{sh}}$ value corresponding to the ith peak in the I(BS) versus α scan. Along the [01$\bar{1}$], $\delta=0°$ azimuth (perpendicular to the close-packed rows), $\alpha_c=16.1°$, while the corresponding rises along the [$\bar{1}$11], $\delta=+90°$ and [1$\bar{1}\bar{1}$], $\delta=-90°$ azimuths occur at $\alpha_c=23.2°$. The larger the interatomic distance between atoms in the scattering plane, the smaller the α_c value at which first-layer atoms lie at the edge of the shadow cones cast by their first-layer neighbors. Since the first-layer atoms occupy symmetrical positions with respect to the [01$\bar{1}$], $\delta=0°$ azimuth, the shadowing effect on these atoms by their first-layer neighbors must be identical along equivalent $\pm\delta$ directions. The close agreement observed in Fig. 4 for the positions of the initial rises in I(BS) along $\pm\delta$ azimuths is therefore proof of the good alignment of the crystallographic axes. The small difference in the intensities of the initial peak for $\delta=\pm12°$ results from inadequate annealing.

C. Scattering structural contour map and plot—SSCM and SSP

I(BS) as a function of α along different crystal azimuths for $-90°\le\delta\le+90°$ are shown as a scattering structural contour map and a three-dimensional scattering structural plot in Figs. 6 and 7, respectively. Since the scans were taken at increments of $\alpha=1°$ or 2° and $\delta=6°$, an interpolation routine was used between the points from adjacent α scans along each δ. The I(BS) values of Figs. 6 and 7 are the experimental intensities, such as those of Fig. 4, multiplied by sinα. This correction accounts for the fact that the area sampled varies as $I_0/\sin\alpha$ as α increases. The critical value of α at low angles, $\alpha^1_{c,\mathrm{sh}}$, is also plotted in Fig. 6.

The SSCM and SSP provide the following information. (i) They are a concise summary of all of the experimental BS data. (ii) They reveal the symmetry of the I(BS) data in (α,δ) space, thereby providing a characteristic identification ("fingerprint") for a specific crystal face ([100], [110], [211], etc.) and type (bcc, fcc, etc.) with minor perturbations due to relaxation and possible major perturbations due to reconstruction. The fingerprint is specific for the particular primary ion type and energy. (iii) They show what general regions of (α,δ) space contain interesting structures for closer, more detailed investigation. (iv) Comparison of the clean surface SSCM and SSP to those of the adsorbate covered surface allows determination of adsorbate-induced reconstruction or relaxation.

Consider the general features of the SSCM and SSP. The contour line at lowest α is due to shadowing of first-layer atoms by their first-layer neighbors. This structure is symmetrical about $\delta=0°$, exhibiting the initial maximum at $10°<\alpha<20°$ for $-80°<\delta<+80°$ and at $\alpha=27°$ for $\delta=\pm90°$. This is confirmation of the crystallographic orientation and the shorter interatomic spacings along the $\delta=\pm90°$ directions. Completely different behavior and very intense structures are observed as α increases above 20° due to scattering from subsurface atomic layers. The extremely high intensities observed for some of these α,δ combinations are due to focusing of the ion trajectories by first- and second-layer W atoms onto third- and fourth-layer W atoms. The asymmetry in these structures is a result of the lack of symmetry between the first and underlying atomic layers, i.e., there is no 180° axis of rotation about the [211] direction and no mirror plane through the $[01\bar{1}]$ azimuth. A line of exceptionally intense peaks runs diagonally across the plots from $\alpha\sim30°$, $\delta\sim-70°$ towards $\alpha\sim75°$, $\delta\sim+80°$. The focusing and channeling created by the first two atomic layers direct the ion trajectories onto subsurface (mainly third and fourth layers) atoms and back out again, resulting in the high intensities observed; examples of this are provided in Sec. III D. Such enhancement of I(BS) due to channeling is opposite from conventional channeling results in which I(BS) decreases due to deep penetration of the projectile ions. The diagonal orientation of these peaks results from focusing of the ion beam onto subsurface layers for $\delta<0°$ at low α; these subsurface layers are shadowed by the outermost layers at high α. For $\delta>0°$, focusing of the ion beam onto subsurface layers occurs at higher α values. If these subsurface layers would be symmetrical with respect to $\delta=0°$, the line of intense peaks in Fig. 6 would be either horizontal or at least symmetrically disposed about $\delta=0°$. Detailed analysis of these peaks requires scrutiny of the crystal structure at the specific α,δ orientations. Examples of this for three specific cases are now considered.

D. Qualitative interpretation of polar incident α angle scans

Three selected I(BS) versus α scans, such as those of Fig. 4, multiplied by sinα, are interpreted in terms of the crystal structure in this section. The specific scans were selected to illustrate a high symmetry azimuth ($\delta=\pm90°$), delineation of first- and second-layer scattering

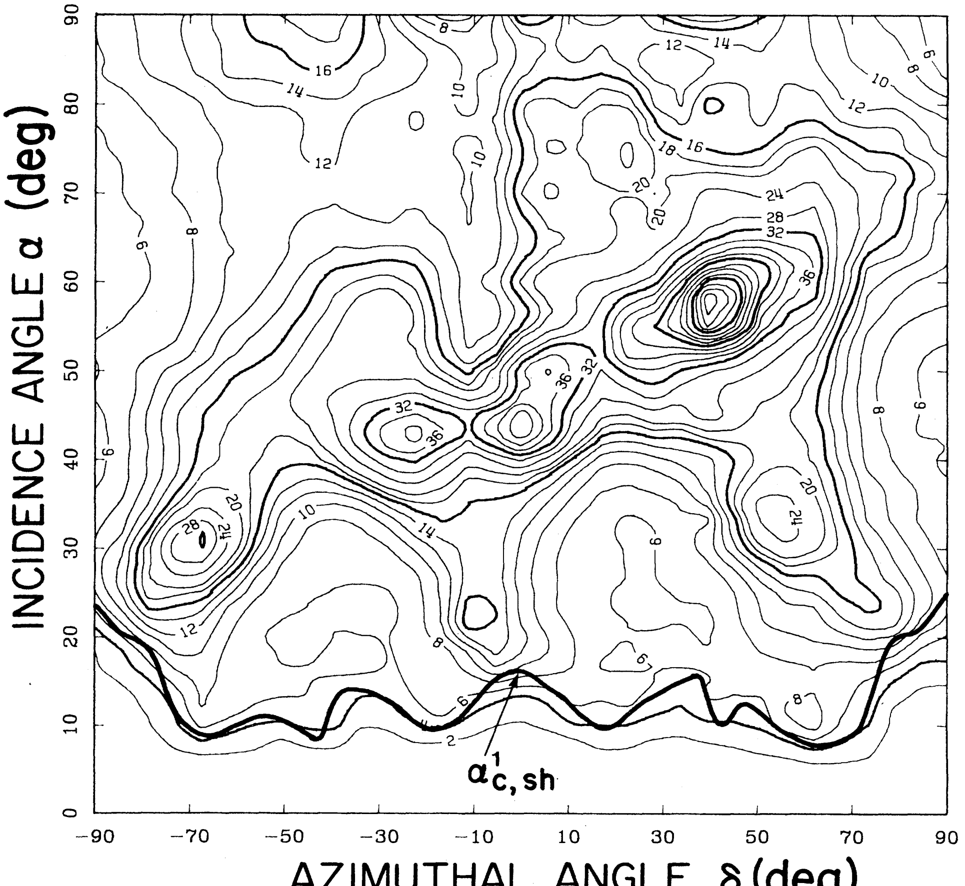

FIG. 6. Scattering structural contour map (SSCM) for the clean W(211) surface. Primary ion: 4-keV Ar$^+$; $\theta=163°$; $\delta=0°$ is the $[01\bar{1}]$ azimuth, $\delta=-90°$ is the $[1\bar{1}\bar{1}]$ azimuth, and $\delta=+90°$ is the $[\bar{1}11]$ azimuth. The critical value of α at low angles, $\alpha_{c,\mathrm{sh}}$, is plotted as a dark solid line.

($\delta=\pm 12°$), and the most intense peak in the SSCM and SSP ($\delta=\pm 42°$). Accompanying each set of scans is a schematic of the W(211) face as observed from the direction of motion of the projectiles,[44,45] i.e., the *ion's eye view*. In such schematics, the incident projectiles move along the normal to the plane of the paper and the outgoing trajectory is in the same azimuth, forming an angle of 17° ($\theta=163°$) with respect to the incoming trajectory, and moving towards the top of the figure.

The $[\bar{1}11]$, $\delta=+90°$ *and* $[1\bar{1}\bar{1}]$, $\delta=-90°$ *azimuths (Fig. 8).* The initial peak at $\alpha=29°$ results from BS from both first- (row) and second- (trough) layer atoms, which cannot be distinguished along these azimuths. An intense peak is observed at $\alpha=75°$, $\delta=+90°$, while along the $\delta=-90°$ azimuth, I(BS) only starts to increase at $\alpha=75°$ and reaches a less intense maximum at $\alpha=83°$. These maxima at high α are due to the onset of BS from the third- and fourth-layer atoms which are shadowed by the first- and second-layers at lower α. Due to the low spatial symmetry of the W(211) surface, the minimum α necessary to have BS from the third and fourth layers along $\delta=\pm 90°$ is different. This is evident from the schematic, where the circles correspond to shadow cones originating on atoms a and 1 of the first layer (dashed circles) and on atoms d and 4 of the second layer (dotted circles), as calculated at a distance equal to the first- and third- and second- and fourth-layer spacings, respectively, along the direction of observation. Along the $\alpha=75°$, $\delta=+90°$ direction, trajectories are focused onto the third- and fourth-layer atoms which are at the edge of the shadow cones *(edge focusing)*,[26] while along the $\delta=-90°$ direction, the third- and fourth-layer atoms are completely shadowed. In the latter case, BS from third- and fourth-layer atoms is not observed until $\alpha=78°$.

The $\delta=\pm 12°$ *azimuths (Fig. 9).* The initial peak due to shadowing of first-layer atoms by their first-layer neighbors is at the same position, $\alpha=15°$, along either $\pm\delta$ direction, although its intensity differs by 25%. This discrepancy is due to slightly different annealing conditions. Two sharp peaks appear at $\alpha=22°$ and 45° along $\delta=-12°$, while along $\delta=+12°$ peaks of high and low in-

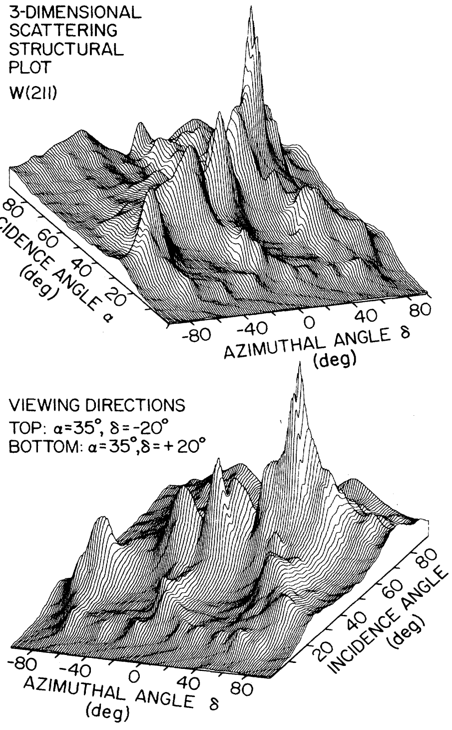

FIG. 7. Three-dimensional scattering structural plot (SSP) for the clean W(211) surface. Viewing directions are $\alpha=35°$, $\delta=-20°$ (top) and $\alpha=35°$, $\delta=20°$ (bottom). Azimuths are defined as in Fig. 6.

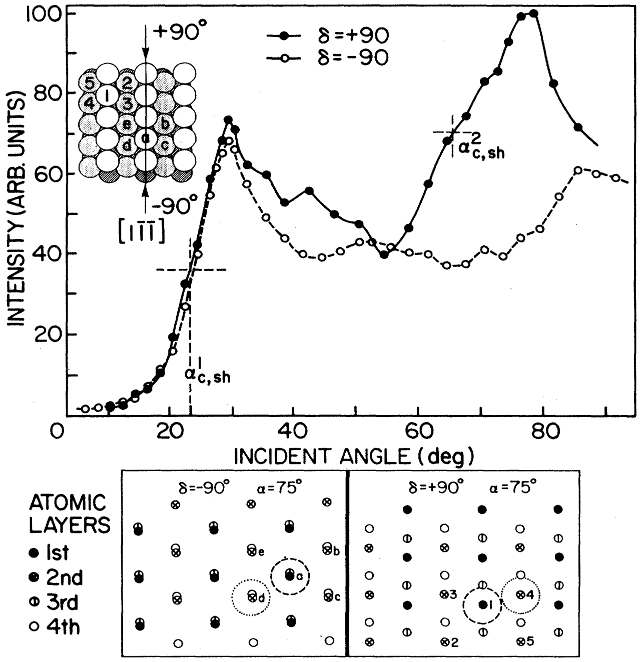

FIG. 8. Polar incident angle α plot of total backscattering (BS) intensity corrected by $\sin\alpha$, i.e., $I(\text{BS})\sin\alpha$, for $\delta=\pm 90°$, $\theta=163°$. The critical angle α_c for first-layer shadowing is indicated. The inset in the upper part of the figure shows the W(211) surface as viewed from the surface perpendicular and the schematic at the bottom of the figure shows the W(211) surface as viewed from the direction of incidence of the primary beam (the ion's eye view). Atoms in different layers of the inset are distinguished as in Fig. 1. Atoms in different layers of the schematic are distinguished as follows: solid circles, first layer; circles with ×, second-layer; circles with vertical line, third layer; open circles, fourth layer. Atoms in the inset and schematic labeled by numbers and letters correspond to a view along $\delta=+90°$ and $-90°$, respectively. Dashed and dotted circles in the schematic correspond to shadow cones of the first- and second-layer atoms, respectively, as calculated at a distance equal to the first- to third- and second- to fourth-layer spacings along the direction of ion incidence. The $\alpha^{i}_{c,\text{sh}}$ positions are indicated on the figure.

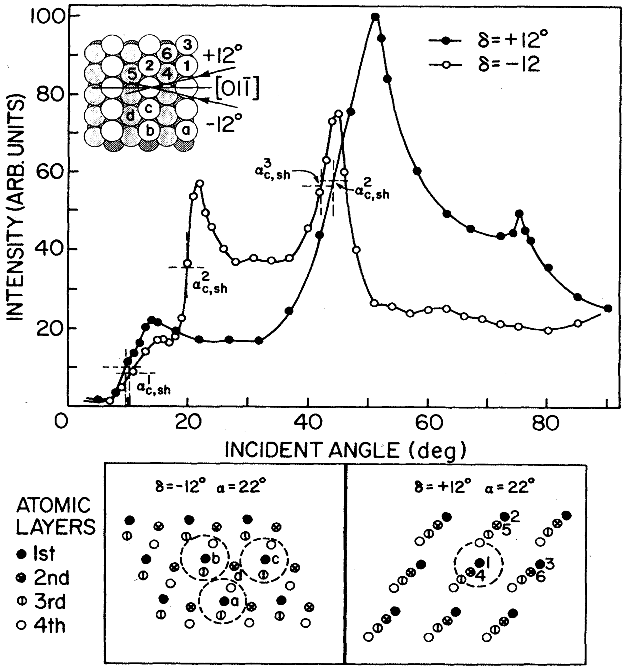

FIG. 9. Same as Fig. 8 for δ=±12°.

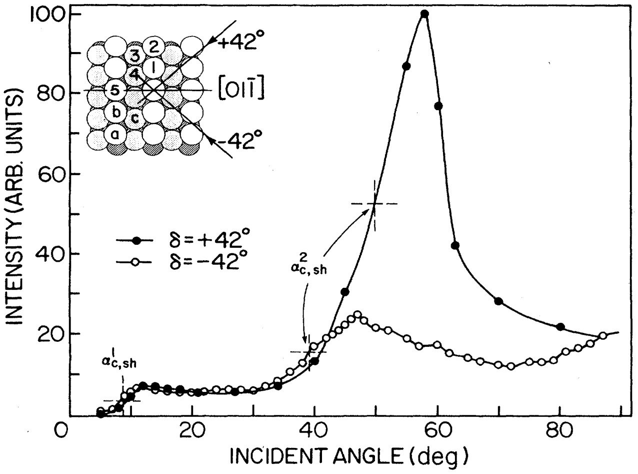

FIG. 10. Same as Fig. 8 for δ=±42°.

tensity appear at $\alpha=50°$ and 75°, respectively. The schematic of Fig. 9 shows that along the $\alpha=22°$, $\delta=-12°$ direction, the projectiles are focused by the shadow cones of the three first-layer atoms *a*, *b*, and *c* onto the second-layer atom *d* which lies near the center of a triangle formed by the cones. This results in a *trigonal hyperchannel*[26] in which the projectile is confined to the indictrix formed by the cones of the three first-layer atoms. The projectiles are focused along their incoming trajectories down onto atom *d* as well as along their outgoing trajectories, resulting in the sharp peak observed at $\alpha=22°$, $\delta=-12°$. A very different situation is observed along $\alpha=22°$, $\delta=+12°$, where the second-layer atom 4 is shadowed by the first-layer atom 1; in fact, along this direction all *n*th-layer atoms lie within the shadow cones of the neighboring $(n-1)$th layer atoms, resulting in the low I(BS) observed in the region $20°<\alpha<35°$. Along this direction, the second-layer atoms begin to emerge from the shadow cones of first-layer atoms at $\alpha=45°$, giving rise to the intense peak at $\alpha=50°$. In a similar manner, the peak at $\alpha=45°$, $\delta=-12°$ can be identified as BS from deeper layers.

The $\delta=\pm 42°$ azimuths (Figs. 10 and 11). The initial peak is at a low α value (11°) due to the large distance between first-layer atoms along this direction. Note, in the inset of Fig. 10, that the critical angle to obtain BS from the first-layer atom 5 is determined by shadowing from both atom 1 and 2. For $\alpha>35°$, I(BS) from both scans increases; the maximum value of I(BS) for all of the α,δ space occurs at $\alpha=58°$, $\delta=+42°$ (see Figs. 6 and 7), while along the $\delta=-42°$ direction I(BS) is 80% lower. These features can be understood from the sequence of changes in the positions of the first- through fourth-layer atoms

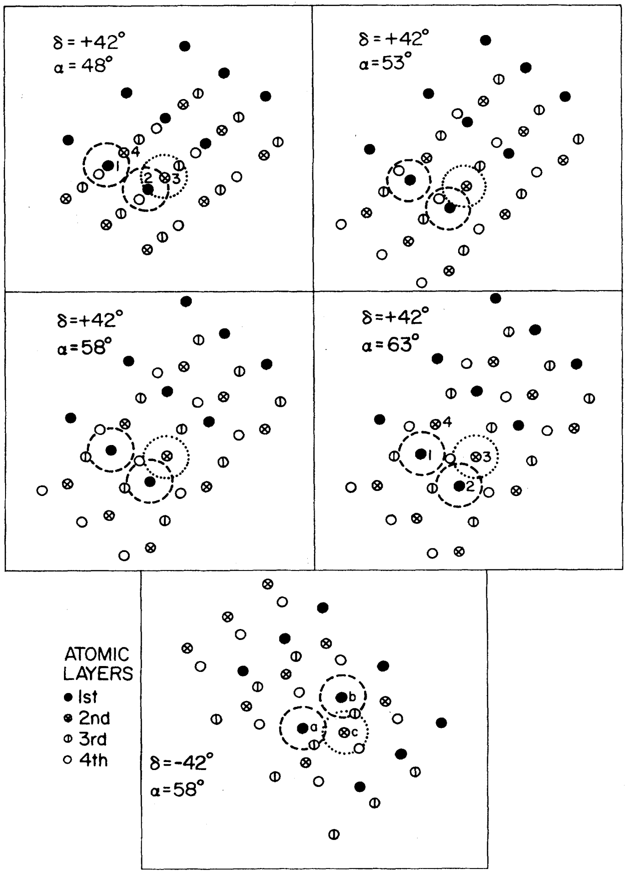

FIG. 11. Sequence of changes in atom positions for δ=+42° and α=48°, 53°, 58°, and 63° (top four figures) and atom positions at δ=−42°, α=58° (bottom figure) as viewed from the direction of incidence of the primary beam (ion's eye view).

with increasing α as shown in Fig. 11. For $\alpha=48°$, $\delta=+42°$, the second-layer atoms (3 and 4) are just at the edge of the shadow cone formed by first-layer atoms (1 and 2) and the third-layer atoms are close to the edge of the shadow cone formed by the second-layer atoms. All of these contribute to I(BS) for $\alpha \geq 48°$; for $\alpha < 48°$, severe shadowing allows BS from only the first-layer. As α increases above 48°, atoms 1 and 2 of the first layer and atom 3 of the second layer form a *trigonal hyperchannel* that focuses projectiles onto fourth-layer atoms. For such a deep channel, similar strong focusing effects also exist along the outgoing trajectories of the reflected particles and these trajectories are not blocked for $\theta=163°$. Such a *double-focusing trigonal hyperchannel* produces the I(BS) maximum at $\alpha=58°$, $\delta=+42°$. For the $\delta=-42°$ azimuth, the I(BS) maximum is at $\alpha=47°$ corresponding to mainly focusing onto second-layer atoms; although some trajectories can be focused onto third- and fourth-layer atoms, their outgoing trajectories are blocked by first- and second-layer atoms (Fig. 11).

E. Ejection β angle scans

In order to obtain data on blocking and focusing effects along the outgoing part of the projectile trajectories, I(FS) was measured as a function of β for specific α,δ orientations as shown in Fig. 12. Such I(FS) versus β scans were performed by holding α constant and varying θ so as to change β according to the relation $\beta=\theta-\alpha$. The $[01\bar{1}]$, $[\bar{1}11]$, and $[11\bar{3}]$ azimuths were chosen for this study because (i) the first-layer interatomic distances along these azimuths (2.74 Å for $[\bar{1}11]$, 4.48 Å for $[01\bar{1}]$, and 5.25 Å for $[11\bar{3}]$) are very different and therefore large differences in the blocking effects are expected and (ii) atoms not located on the selected crystal azimuths should produce only small deflections of the projectile trajectories. The incident angles were chosen just above the $\alpha^1_{c,\mathrm{sh}}$ value for each azimuth in order to avoid shadowing effects, focus a large number of trajectories onto the atoms of interest, and minimize the contributions from deeper atomic layers. The Ar I(FS) versus β scans are shown in Fig. 12 for these three azimuths. A log-log plot was used in order to emphasize the low-β structure and factor-of-10^2 change in I(FS). These β curves exhibit a steep rise at low β, reach a maximum, and then decrease monotonically with increasing β. The critical β_c positions were taken as one-half the peak height minus the background. The increase in β_c along azimuths with decreasing interatomic distance between neighboring W atoms is due to the increased blocking along these azimuths.

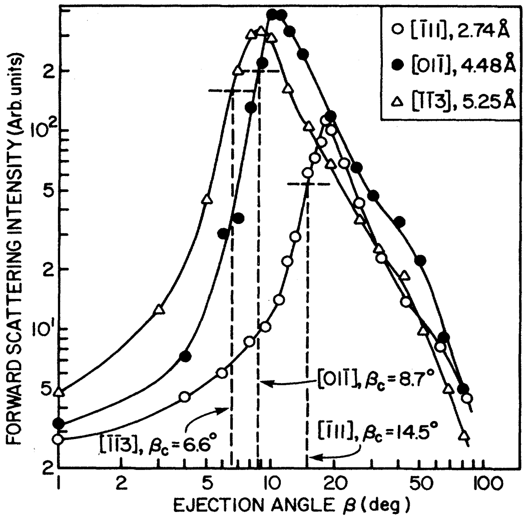

FIG. 12. Plots of forward scattering intensity I(FS) vs ejection angle β along the $[01\bar{1}]$, $[\bar{1}11]$, and $[11\bar{3}]$ azimuths obtained by varying θ at fixed α and using the relation $\beta=\theta-\alpha$. The critical ejection angles β_c and first-layer interatomic spacings are indicated. Primary ion: 4-keV Ar^+; incident angles used are $\alpha=20°$ for $[01\bar{1}]$, $\alpha=27°$ for $[\bar{1}11]$, and $\alpha=18°$ for $[11\bar{3}]$.

IV. COMPUTER SIMULATIONS

The simple geometrical arguments presented in Sec. III are sufficient for a qualitative interpretation of the scattering results. In order to obtain quantitative information about the structure, the experimental data have been compared to three different types of computations: (1) single-atom shadow-cone calculations, (2) multiatom classical trajectory simulations, and (3) BS flux distributions. This section describes the computational procedures and provides results for calibration of the scattering potentials and vibrational amplitudes.

A. Single-atom shadow cone calculations

The dependence of the shadow cone radius $R(L)$ on the distance L behind the shadowing atom was computed from the envelope of projectile trajectories around a single target atom.[44] This expression was used specifically for 4-keV Ar^+ scattering from a single W atom, yielding a shadow cone in the center-of-mass coordinate system. The interaction between Ar^+ and W atoms is approximated by both the Molière[26] (M) and the Biersack-Ziegler[27] (BZ) potentials. For both of these potentials, the scaling factor C of the potential screening length was adjusted to yield the best least-squares fit between the computed values and experimental points on the shadow cone radii. The experimental points on the shadow cone were determined as follows. The critical angles α_c for the onset of $\theta=163°$ backscattering from first-layer atoms were measured from polar incident angle scans along the $[\bar{1}11]$, $[1\bar{1}\bar{1}]$, $[01\bar{1}]$, $[11\bar{3}]$, $[\bar{1}\bar{1}3]$, $[10\bar{2}]$, and $[\bar{1}02]$ azimuths. The experimental values of R and L were then calculated as $R=a\sin\alpha_c+p$ and $L=a\cos\alpha_c$, where a is the first-layer interatomic distance, taken as the bulk spacing, along the corresponding azimuth. The optimized values of C for fitting the potentials to the seven experimental shadow cone points were found to be $C_M=0.94$ and $C_{\mathrm{BZ}}=0.99$. Comparison of the seven experimental points with the calculated shadow cones in Fig. 13 shows that both potentials generate essentially identical shadow cones that are in excellent agreement with the experimental data. Figure 14 shows three different cuts through planes perpendicular to the (211)

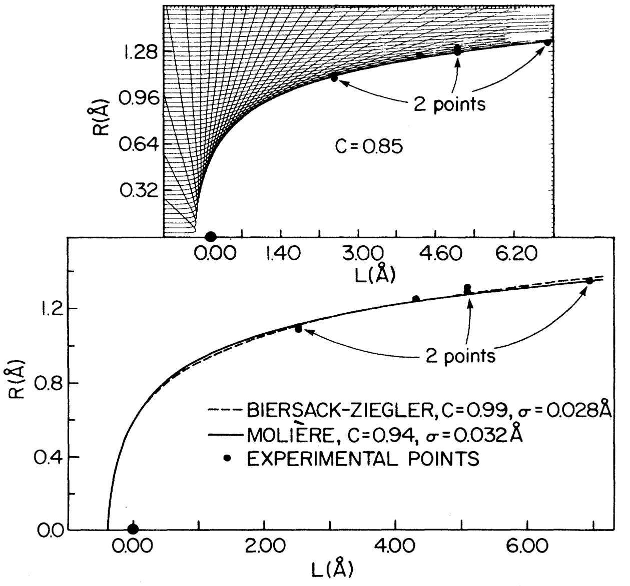

FIG. 13. Trajectory simulations of shadow cones (upper figure) using the Biersack-Ziegler (BZ) potential and calculated shadow cone curves (Refs. 44 and 46) (lower figure) using both the BZ and Molière (M) potentials for 4-keV Ar^+ scattering from W. The seven experimental points are determined from I(BS) vs α scans for first-layer shadowing. The scaling factor C in the screening length was adjusted to give the best fit of the shadow cones to the experimental points. σ is the standard deviation of the points from the shadow cone.

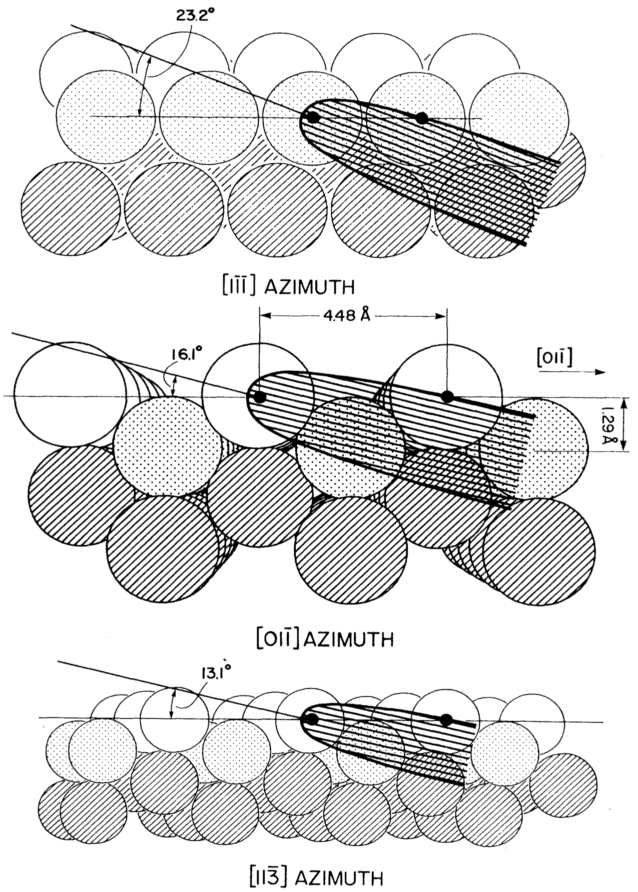

FIG. 14. Cuts through planes perpendicular to the (211) face along three different azimuths showing calculated shadow cones drawn to scale and oriented at α_c.

face with calculated shadow cones drawn to scale and oriented at α_c. The edges of the shadow cones cross directly over the neighboring atomic centers when oriented at α_c.

Calibration of the shadow cones by measurement of α_c for first-layer scattering along different azimuths, as described above, is possible because the first-layer is only relaxed and not reconstructed. Therefore the interatomic spacings between first-layer atoms remain as in the bulk and can be used for calibration. For a reconstructed surface (e.g., with the interrow spacings along the $[01\bar{1}]$ direction increased, decreased, or both, or with different interatomic spacings along the $[1\bar{1}\bar{1}]$ direction) it would not be possible to find a single value of C that would provide a fit to the cone along several azimuths by using the bulk (unreconstructed) spacings. The differences in the bulk and reconstructed spacings would be a function of the azimuthal direction, yielding a poor fit of experimental points to the calculated cone. The fact that all seven experimental points are in excellent agreement with the calculated cone (Fig. 13) indicates that there is no reconstruction, only relaxation in a manner in which the first-layer interatomic spacings are the same as in the bulk. If there are no known interatomic spacings for a specific crystal face, calibration of the cones can be accomplished on other faces of the same crystal for which some interatomic spacings are known. On the other hand, tests of the potential on known surface structures using $C_M = 1.0$ showed[4] that the experimental interatomic distances were reproducible to within an error margin of $\sim 7\%$.

B. Multiatom trajectory simulations

1. *Shadowing*

Two-dimensional trajectory simulations were carried out by solving Hamilton's equations of motion for 4-keV Ar^+ projectiles impinging on a finite two-dimensional slice of the W lattice. As described elsewhere,[46] the equations of motion are integrated by a fourth-order predictor-corrector technique with self-adapted integration step. For each set of initial conditions, the integration is continued until the projectile velocity becomes constant in magnitude and direction. The interactive potential for each projectile is represented by a sum of binary BZ potentials. The potential was calibrated by varying the scaling factor C until the average distance between the seven experimental R,L points and the trajectories at the edge of the shadow cone was minimized for the case where the maximum value of θ for the BS trajectories reaches 163°. The optimized value of C obtained by this method was $C = 0.85$; comparison between the trajectories and experimental points is shown in Fig. 13. Examples of calculated trajectories for 4-keV Ar^+ scattering along the $[1\bar{1}\bar{1}]$ azimuth in Fig. 15 shows that only FS is obtained for low α and that 163° BS occurs at $\alpha \sim 23°$, in agreement with the experimental result of Fig. 8.

2. *Blocking*

Examples of blocking cones, calculated as above using the previously optimized value of C, are shown in Fig. 16 for 4-keV Ar^+ FS along the three different azimuths used in Fig. 12. The α_c values corresponding to those used in the I(FS) versus β measurements of Fig. 12 are used. It can be seen that the trajectories that are FS into small β are also deflected by the neighboring atom, forming a blocking cone. The semiaperture of these blocking cones depends on the energy and type of colliding particles, as for shadow cones. However, since the trajectories of atoms scattered from the neighboring atom are diverging rather than parallel, the semiaperture of blocking cones is also dependent on the incident angle and the interatomic distance. The calculated minimum exit angles β_c at which FS can be observed along the three azimuths in Fig. 16 are in good agreement with the β_c values determined from the sharp rises of the $I(FS)$ versus β plots of Fig. 12. This result shows that the potential function calibrated from the shadow cones can be used to calculate blocking cones that are in good agreement with experimental measurements.

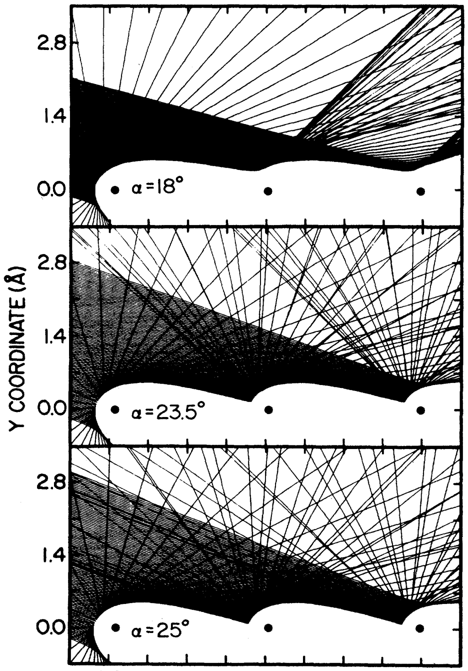

FIG. 15. Examples of calculated trajectories for 4-keV Ar^+ scattering along the $[1\bar{1}\bar{1}]$ azimuth of W showing the sensitivity of BS to small changes in α.

C. BS flux distributions

The BS flux distributions as a function of α were calculated according to the method of Daley, Huang, and Williams.[47] This method calculates the relative hitting probability of an atom in a flux of projectiles that has been deflected by another atom using the Molière potential. This probability is sensitive to the relative thermal vibrational amplitude of the atoms in the crystal. The calculated shadowing interactions can be combined to simulate an incident angle scan, i.e., I(BS) versus α. In applying this calculation, d was fixed according to the first-layer interatomic spacings along a given azimuth while the screening constant C of the potential and the vibrational amplitude Z of the atoms were varied in order to obtain the best fit to the α_c values of the I(BS) versus α scans for first-layer scattering. These calibrated values of C and Z that provided the best fits to the experimental data, as shown in Fig. 17, were 0.85 and 0.13 Å, respectively. The calculated flux distributions for first-layer scattering based on these C and Z values yield α_c values that are all within 1° of the experimental α_c's. The bulk Z value at 20 °C, calculated[48] from the Debye temperature, is 0.084

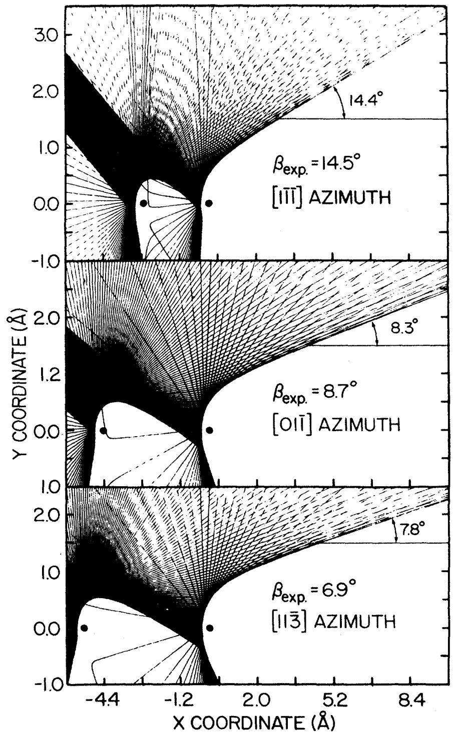

FIG. 16. Examples of blocking cones for 4-keV Ar^+ scattering from W along the three azimuths and incident angles used in Fig. 12. The apparent asymmetry in the shape of the cones is a result of different scales on the abscissa and ordinate. The calculated and experimental (from Fig. 12) values of β_c are indicated. Projectiles impinge from the upper left along the dark band of impact parameters p and scatter from the atom on the left. FS trajectories are blocked by the atom on the right, forming a blocking cone.

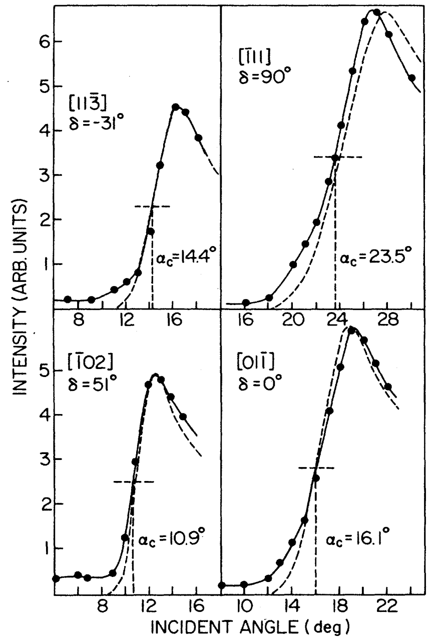

FIG. 17. Calculated (dashed lines) and experimental (points and solid lines) I(BS) vs α distributions for 4-keV Ar^+ scattering from W(211) along the $[1\bar{1}\bar{3}]$, $[\bar{1}11]$, $[\bar{1}02]$, $[01\bar{1}]$ azimuths for $\theta=163°$.

Å. The high-Z value obtained from the flux distributions suggests that the surface vibrational amplitude is larger than that of the bulk. The experimental I(BS) values are considerably higher than the calculated flux distributions for α values less than α_c. This is caused by two factors. First, I(BS) versus α scans were started immediately after annealing while the sample was $\approx 300\,°C$; this procedure provided a clean surface throughout the entire set of measurements. The temperature of the sample during these scans decreased from $\approx 300\,°C$ at low α to room temperature at high α. This elevated temperature contributes to broadening of the I(BS) versus α curves, particularly at low α where the sample temperature is highest. Second, the background from first-layer scattering, which decreases as α increases, underlies the beginning of second-layer scattering, an effect which is not included in the flux density calculations.

V. SURFACE RELAXATION

The geometry of the two outermost atomic layers of the (211) surface are considered in this section. Determination of the registry of the first and second layers can be obtained from experimental measurements alone without the use of the above calculations, while determination of the first- to second-layer spacing requires application of the calibrated calculations.

A. Lateral relaxation (change in layer registry) of the first-atomic layer

The extreme sensitivity of the technique to details of the surface structure can be used for direct determination of the first- and second-layer registry. The lack of a plane of symmetry containing the $[01\bar{1}]$ azimuth for the (211) surface results in asymmetrical scattering structures from subsurface layers along $\pm\delta$ directions. Shifts in the first- and second-layer registry or lateral relaxation can be detected by carefully monitoring the α_c values for second-layer scattering along directions near those azimuths for which the first-layer atoms are expected, from the bulk structure, to be directly aligned with the second-layer atoms. The α_c values should be maximum for those δ values where the first- and second-layer neighboring atoms are aligned. For the bulk-truncated surface (inset of Fig. 18), the first- and second-layer nearest neighbors are aligned for $\delta=22.2°$ and $-39.2°$. Values of α_c for second-layer scattering were carefully measured in a range of $\pm 5°$ about these two expected δ values. The results are shown in Fig. 18 as plots of I(BS) versus α from which the α_c values obtained are plotted as α_c versus δ. The two I(BS) versus α plots shown are along the azimuths that yield the maximum α_c values. The maximum α_c values occur at $\delta=24.0°$ and $-37.5°$, which are 1.9° higher and 1.7° lower, respectively, than the azimuths expected from the bulk-truncated surface. Using these experimentally determined $\pm\delta$ values for first- and second-layer atom alignment, and assuming that the shift occurs only along the $[1\bar{1}\bar{1}]$ azimuth, the first- and second-layer registry can be calculated from simple geometry. The result (inset of Fig. 18) shows that the lateral distance from the center of a second-layer atom to the center of a first-layer atom is 1.00 ± 0.07 Å (bulk value 0.91 Å) along the $[1\bar{1}\bar{1}]$ azimuth and 1.72 ± 0.07 Å (bulk value 1.83 Å) along the $[\bar{1}11]$ azimuth (see inset of Fig. 18). This lateral relaxation of 0.10 Å is in excellent agreement with the LEED prediction[32] of 0.09 Å. This shift brings the center of the first-layer atoms nearer to the symmetrical bridge position between two second-layer atoms.

In Fig. 18 the α_c versus δ plots are not symmetrical about the maximum α_c values and the I(BS) versus α curve for $\delta=-37.5°$ exhibits two maxima. These results are due to the emergence of the third- and fourth-layer atoms out of the first- and second-layer shadow cones in an asymmetrical manner as α and δ are rotated. As a result, the data from $\delta=24.0°$ are more reliable than the data from $\delta=-37.5°$ in determination of the lateral relaxation, as will be detailed in Sec. V C.

B. Vertical relaxation (change in first- and second-layer spacing)

The experimental α_c values determined along the $\delta=24.0°$ and $-37.5°$ azimuths and the relaxed horizontal layer registry were used in determination of the first- to second-layer vertical spacing. Since the first- and second-layer atoms are aligned along these δ directions, the two-dimensional calculations can be applied to determination of the layer spacing. All three methods of calculation described in Sec. IV were used for this determination. The sensitivity of the first- to second-layer spacing to changes in α_c is ~0.03 Å/deg.

In the first method, the optimized Molière potential

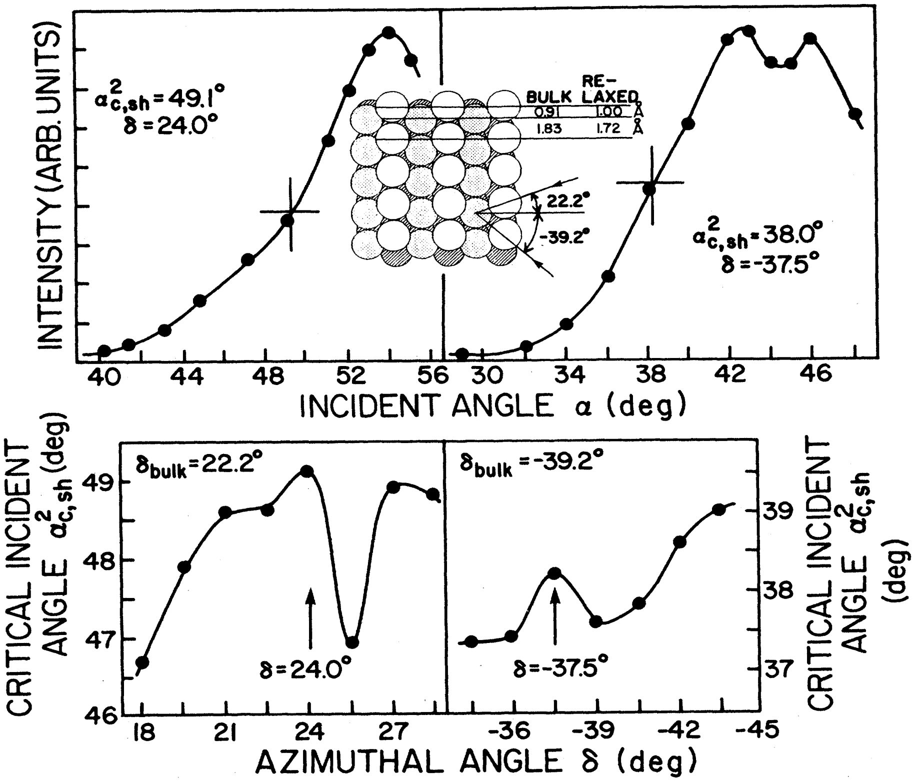

FIG. 18. Upper: plots of I(BS) vs α along the azimuths $\delta = 24.0°$ and $-37.5°$ that yield the maximum $\alpha^2_{c,\mathrm{sh}}$ values for second-layer scattering. Lower: plots of $\alpha^2_{c,\mathrm{sh}}$ (determined from curves such as in the upper part) vs δ (in the region near the expected first- and second-layer nearest-neighbor alignment) showing the δ values corresponding to the maximum $\alpha^2_{c,\mathrm{sh}}$'s. The inset in the upper part shows the $\pm\delta$ values for alignment of the bulk truncated structure and the lateral shift of the first layer with respect to the second layer.

was employed to calculate the shadow cone as shown schematically in Fig. 19. The horizontal coordinate A was taken from the crystal geometry, assuming 0.10 Å lateral relaxation as determined in Sec. V A. Since the experimental α_c's for second-layer scattering, the positions A along the azimuths, and the shape of the shadow cone are known, it is possible to calculate analytically the vertical position d of the second-layer atom. As seen from Fig. 19, $d = b + c$, where b is the distance $\overline{A}\,\overline{B}$ from the surface to the shadow cone taken along the normal to the surface passing through A and c is a correction due to the use of $\theta < 180°$. The coordinates for point B were obtained from the intersection of the calculated shadow cone R and the normal to the surface passing through A, defined by

$$R = -\tan(\pi/2 - \alpha^2_{c,\mathrm{sh}})L + A/\sin\alpha^2_{c,\mathrm{sh}} . \qquad (2)$$

The correction c can be approximated by $c = p/\cos\alpha_c$, where $p = 0.037$ Å is the impact parameter corresponding to a 4-keV Ar-W collision with $\theta = 163°$. The values of d obtained from this method are listed in Table II.

In the second method, ion trajectories were computed along each azimuth with α equal to the experimentally determined α_c. The second-layer atom was located at the coordinates A,d (see Fig. 19); the vertical coordinate d was allowed to vary until the maximum θ of the BS trajectories reached 163°. The sensitivity of the trajectory calculations to d is shown in Fig. 20 and the d values obtained in this manner are listed in Table II.

In the third method, BS flux distributions using the optimized C and Z values were employed to simulate second-layer scattering along the two azimuths. The d values were varied in order to obtain the best fit to the ex-

TABLE II. Values of the first- to second-atomic layer spacing determined from TOF-SARS. The bulk first to second atomic layer spacing is 1.29 Å.

Method of calculation	First- to second- layer spacing (in Å) 24.0° azimuth	−37.5° azimuth[a]
Shadow cone calculations	1.18±0.10	0.81
Trajectory simulations	1.17±0.05	0.80
(BS) flux distributions	1.15±0.07	

[a] Values of the first to second atomic layer spacing determined along this azimuth are too short due to interferences from deep layer scattering in the α_c determination (Sec. V B).

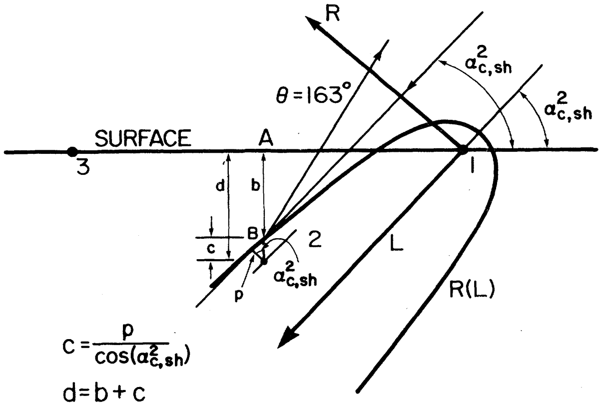

FIG. 19. Schematic diagram showing the use of the calculated shadow cone and experimental $\alpha^2_{c,\mathrm{sh}}$ value measured for second-layer scattering to determine the first- to second-layer spacing. Atoms 1 and 3 are in the first layer, atom 2 is in the second layer, c is the correction introduced by the impact parameter p, and the first- to second-layer spacing is $d=b+c$. The shadow cone coordinates are labeled R and L.

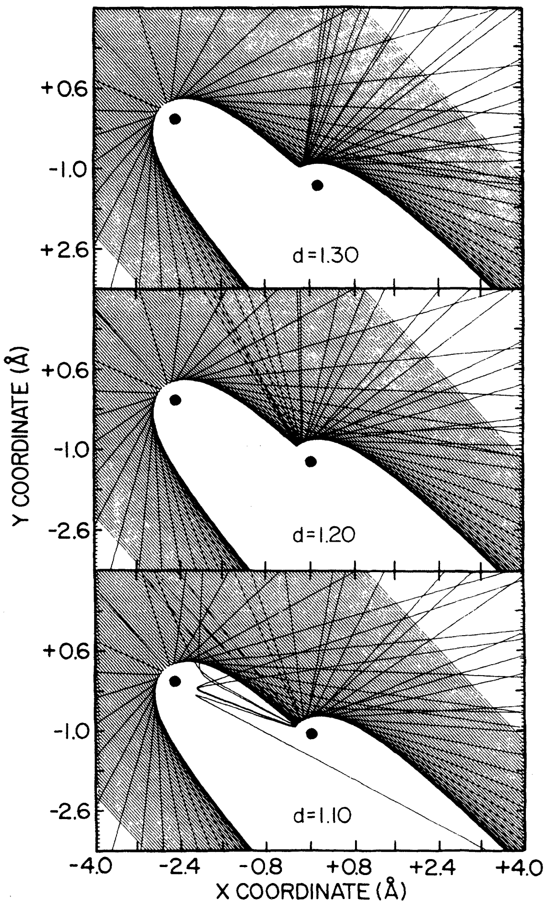

FIG. 20. Examples of calculated trajectories for 4-keV Ar^+ scattering along the $\delta=24.0°$ azimuth with α fixed at $\alpha^2_{c,\mathrm{sh}}$ (49.1°) showing the sensitivity of BS to small changes in first- to second-layer spacing d.

perimental results. The computed and experimental distributions are compared in Fig. 21 and the values of d obtained are listed in Table II. Along the $\delta=24.0°$ azimuth, contributions to I(BS) from second-layer scattering, third- plus fourth-layer scattering, and the combined total from these three levels are shown. The third- and fourth-layer scattering, have been included here because, as observed in the ion's eye view schematic at $\delta=24.0°$, $\alpha=49.1°$, the first- through fourth-layer atoms are nearly aligned such that scattering from these deeper layers can occur at α values that are only slightly larger than that of second-layer scattering. Therefore all of these contributions combine to form the experimentally observed distribution. The α_c value for the combined total scattering curve is $\sim 1°$ from the experimental value. Interferences from deeper layers are more significant at $\delta=-37.5°$, as will be shown in Sec. V C.

The results of the three methods of calculation, summarized in Table I, show that the average first- to second-layer spacing d is determined to be 1.17 ± 0.07 Å and 0.84 Å along $\delta=24.0°$ and $-37.5°$, respectively. The d value determined at 24.0° is the accepted value of the vertical relaxation. The d value calculated from the $-37.5°$ data is not used because of the interference from deep layer scattering as discussed below. Nevertheless, the $-37.5°$ data qualitatively predict relaxation in the same direction as the quantitatively accurate value determined at 24.0°. The consistency in the d values at 24.0° produced by the three different methods of calculation lends confidence in the experimental and computational procedures. The contraction of 0.12 Å is in good agreement with the LEED prediction[32] of 0.16 Å. It is noted that the reproducibility of the first-layer interatomic spacings using the calibrated computations is within 0.05 Å; the major uncertainty in determination of the first- to second-layer spacing results from interference due to third- and fourth-layer atoms that are nearly aligned with the second-layer atoms.

C. Interferences from deep layers

Scattering from deep (third and fourth) layers that occurs at approximately the same α value as first- and second-layer scattering can interfere with the determination of interatomic spacings. For example, along the $\delta=-37.5°$ azimuth, two maxima are observed as shown in Fig. 21. Calculated flux distributions for the second-layer, third plus fourth-layers, and combined total are shown; the maximum of the latter distribution is shifted by $\approx 4°$ and 8° towards higher α from the second and first maxima, respectively, of the experimental distribution. These discrepancies are well outside of the uncertainties in the experiments and calculations and are a result of focusing from first-layer atoms onto fourth-layer atoms as shown in the schematic of Fig. 21 at $\delta=-37.5°$, $\alpha=38.2°$. Shadow cones are shown around first-layer atoms (1) with radii corresponding to their sizes at the first- to second-layer (dotted) and first- to fourth-layer (dashed) spacings. Note the edges of the first- and second-layer and first- and fourth-layer cones are approximately over both the second-layer atom (3) and the fourth-layer atom (2). As a result, trajectories are fo-

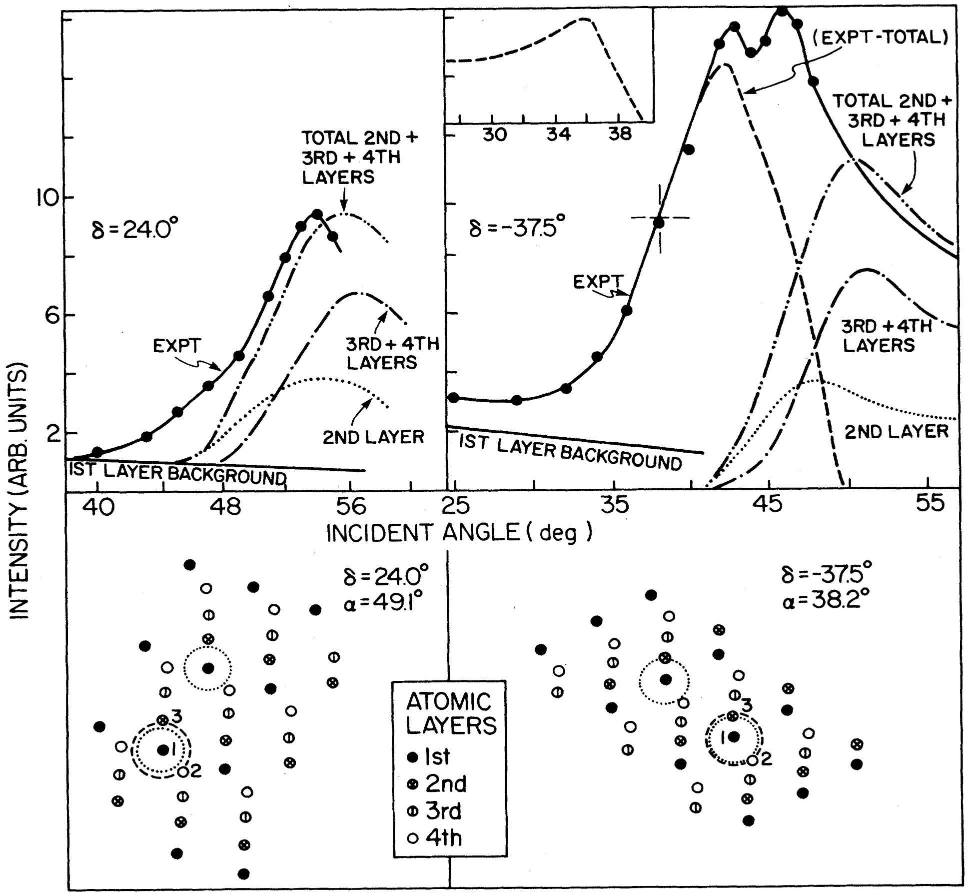

FIG. 21. Polar incident angle plots I(BS) vs α (points plus solid line) for $\delta=24.0°$ and $-37.5°$ in the α range corresponding to second-layer scattering. Calculated contributions to I(BS) from second-layer scattering (· · · ·), third- plus fourth-layer scattering (—·—), and the sum of these three layer contributions (—·—·—·) are indicated. Contributions from the second and third plus fourth layers are weighted as 1:2 based on the number of scattering centers. For $\delta=-37.5°$, structure (— — —) corresponding to first- and fourth-layer focusing is indicated. The schematics at the bottom of the figure show the surface as viewed from the direction of incidence of the primary beam (the ion's eye view). Atoms in different layers are distinguished as in Fig. 8. Dotted and dashed circles in the schematic correspond to shadow cones of the first-layer atoms as calculated at a distance equal to the first- to second- and first- to fourth-layer spacings, respectively, along the direction of ion incidence. The inset (upper center) shows a calculated I(BS) vs α scan for fourth-layer atoms moving into (rather than out of) the shadow cones of first-layer atoms, illustrating the mirror-image effect.

cused from first-layer atom cones onto both second- and fourth-layer atoms at about the same α values. This produces second- and fourth-layer scattering peaks at α values that are very close to each other; the two maxima in the α scan at $\delta=-37.5°$ correspond to these peaks. Note that this is not the case at $\delta=24.0°$, $\alpha=49.1°$; in this case the second-layer atom is completely outside of the first- and second-layer cone while the fourth-layer atom is still partially inside of the first- and fourth-layer cone, resulting in second-layer scattering at lower α than fourth-layer scattering.

The dashed line in Fig. 21 for $\delta=-37.5°$ obtained from subtracting the total calculated curve from the experimental curve describes the contribution from focusing onto deeper levels as described above. Note that the shape of this dashed line peak is a mirror image of the typical shapes observed in the I(BS) versus α scans, e.g., Figs. 4 and 8–10. In these typical scans, the neighboring atoms are moving *out* of the cones as α increases. For focusing onto the deeper levels, the fourth-layer atoms are moving *into* the first-layer cones as α increases. The inset (upper center) of Fig. 21 illustrates this mirror image effect in an I(BS) versus α scan calculated for a fourth-layer atom moving into the cone of a first-layer atom. The flux distribution calculations cannot accurately reproduce these experimental distributions because the atoms in question in the schematics of Fig. 21 do not all lie in the same plane and the calculations cannot handle these three-dimensional structures.

VI. DISCUSSION

The W(211) surface has provided an excellent test case for the structural capabilities of TOF-SARS. The anisotropy of the row-trough structure and the lack of a plane of symmetry along the $[01\bar{1}]$ azimuth results in large variations in the I(BS) and I(FS) versus α scans for different δ

values. The low symmetry of this surface therefore results in many scattering details which are unique to this structure. Although these details make the interpretation more complicated, they are useful in analysis of surface relaxation and adsorbate-site positions.[37,38] This is clearly depicted in the scattering structural contour maps and scattering structural plots, which are representative of the bcc(211) structure. The demonstrated sensitivity of the technique to details of the first- through fourth-layer atomic structure, excellent reproducibility and precision with which the measurements can be made, and simplicity of the interpretations suggests that TOF-SARS has tremendous potential as a surface crystallographic technique. Since it provides direct measurements of interatomic distances in surfaces, it should be complementary to LEED which provides the symmetry of surface structures (long-range structure). The high annealing temperature required and the difficulty in maintaining an atomically clean surface make tungsten a challenging system to study. The fact that these difficulties have been successfully overcome indicates that application of TOF-SARS to many other surfaces should be feasible.

One of the major advantages of TOF-SARS is the ability to derive structural information directly from experimental data (such as lateral relaxation, Sec. V A) and from simple calculations (such as vertical relaxation, Sec. V B). All of the computations reported herein were carried out on laboratory minicomputers. The agreement between the first- to second-layer spacings obtained from the three different methods of computation lends confidence to the calculated vertical relaxation value and the reliability of the computational procedures. Nevertheless, these procedures are only two-dimensional simulations and they are not capable of treating the hyperchanneling processes (Sec. III C) that dominate the SSCM and SSP in certain α,δ regions; complete three-dimensional simulations are required for treating these phenomena.

The experimental α_c values were all measured at a position of 50% of the total peak height minus the background in the I(BS) versus α scans and the potential screening functions of the shadow-cone calculations were calibrated to obtain the best fit at this position. In the BS flux distribution calculations, both the screening constant and the vibrational amplitudes were varied in order to get the best agreement with the experimental I(BS) versus α distributions at the 50% peak height position. The choice of 50% of the peak height for α_c is arbitrary. Previous publications[3-22] have used values ranging from 50% to 80%. For an ideal step function there is, of course, only one position; however, effects such as vibrational motions, focusing, and surface roughness (especially at low α) tend to broaden the I(BS) versus α steps. The effect of the choice of the α_c position on determination of interatomic spacings using both calibrated and uncalibrated shadow cones is presently being investigated in this laboratory.

All of the results reported herein are based on 4-keV Ar^+ primary ions. This energy and ion were chosen in order to provide sufficient energy for detection of neutrals in the BS geometry and large shadow cones to emphasize the first- to second-layer sensitivity. Some experiments were also carried out with Ne^+ ions; the results were comparable to the Ar^+ results with the exception that the α_c values were lower by 1°–3° due to the $\approx 15-20\,\%$ smaller Ne^+/W shadow cone. Although heavy target atoms such as W can be analyzed by either Ne^+ or Ar^+ scattering, this is not the case for light targets. Ne^+, Li^+, and He^+ scattering are more desirable for light targets due to the lower momentum transfer and resulting damage. For second-row elements, He^+ and Li^+ scattering provide the best results, although due to the small size of the He^+ shadow cones, scattering can occur from several atomic layers resulting in complicated spectra. Structural analysis of first- through third-row elements can be carried out by recoiling as described in II (Ref. 37) and III.[38]

In comparison of the TOF technique with detection of both neutrals and ions to electrostatic analysis with detection of only ions, we note the following. It is well known[49] for H^+ and He^+ scattering that measurements of neutrals plus ions produce broader peaks than measurements of ions only due to the high degree of neutralization as these light ions penetrate and then return to the surface. For Ne^+ and Ar^+ scattering, the widths of the neutral plus ion and ion only peaks are nearly identical. Also for these ions, measurements[39] of scattered ion fractions as a function of α show that the ion fractions are not highly sensitive to α on the clean W surface; thus the degree of neutralization of $\mathrm{Ne}^\pm$ and Ar^+ in first- through fourth-layer scattering is relatively constant.

The present limitations of TOF-SARS for determining reconstructed and relaxed surface structures are as follows.

(i) The technique is rather slow. A single I(BS) versus α scan can be made in ~ 15 min, although collection of an entire SSCM including reannealing time requires about 20–25 h. Individual scans along certain azimuths may be sufficient for many structural determination cases.

(ii) The limited resolution of TOF analysis precludes separation of BS peaks from alloy and compound surfaces whose constituents are heavy atoms of similar masses.

(iii) Determination of long interatomic distances, e.g., $\gtrsim 7$ Å, using projectiles for which the shadow-cone radii are ~ 1 Å results in α_c values that are so low that the edges of the shadow cones are nearly parallel to the surface. This situation can be improved by using lower energy projectiles which have larger shadow cones.

(iv) depending on the specific surface structure, scattering contributions from subsurface (third and fourth) layers can interfere with the accuracy of the results for measurements of vertical and lateral first- to second-layer spacings.

(v) The results can be complicated by the existence of domains with differing orientations.

VII. SUMMARY AND CONCLUSION

The specific results of this study can be serialized as follows.

(i) The demonstrated high sensitivity of the TOF-SARS technique, rendered by TOF analysis and detection of both ions and neutrals, allows determination of surface crystal structures to an accuracy of <0.1 Å.

(ii) Relaxation of the clean W(211) surface has been detected and quantified in three dimensions; the values determined for the first- to second-layer spacing are as follows: vertical spacing, 1.17 ± 0.07 Å; lateral spacing from the center of the second-layer atom to the center of the first-atom, 1.00 ± 0.07 Å along $[1\bar{1}\bar{1}]$ and 1.72 ± 0.07 Å along $[\bar{1}11]$. This represents a vertical contraction of 0.12 ± 0.07 Å (9.3%) and a lateral shift of 0.10 ± 0.07 Å (3.6%) along the $[1\bar{1}\bar{1}]$ azimuth from the bulk-truncated surface.

(iii) Scattering structural contour maps and scattering structural plots represent the W(211) surface symmetry in (α,δ) space.

(iv) Simple shadowing and blocking cone, trajectory simulation, and BS flux distribution calculations performed on laboratory minicomputers and calibrated to known interatomic spacings are adequate for interpretation of many of the observed scattering features and determination of surface relaxation or reconstruction.

(v) Structures associated with scattering of these low-energy ions from the first through fourth atomic layers have been delineated; scattering features from the third and fourth layers are often emphasized at high α values due to channeling phenomena.

ACKNOWLEDGMENTS

The authors are grateful to R. R. Rye (Sandia Laboratories, Albuquerque, NM) for initially stimulating our interest in the W(211) surface, for providing the crystal, and for many helpful discussions. We appreciate the help of Y. Lifshitz, F. Masson, and R. R. Rye for critically reading the manuscript. We thank R. S. Williams, R. S. Daley, and J. H. Huang (UCLA) for providing a copy of their hitting probability program. This material is based on work supported by the National Science Foundation under Grant No. CHE-88-14337 and by the Texas Advanced Research Program.

---

*Permanent address: Universidad Nacional del Comahue, Centro Regional Bariloche, 8400 San Carlos de Bariloche, Rio Negro, Argentina.

[1] D. P. Smith, J. Appl. Phys. **38**, 340 (1967).

[2] For a recent review, see Th. Fauster, Vacuum **38**, 129 (1988).

[3] M. Aono, Y. Hou, C. Oshima, and Y. Ishizawa, Phys. Rev. Lett. **49**, 567 (1982).

[4] M. Aono, Y. Hou, R. Souda, C. Oshima, S. Otani, and Y. Ishizawa, Phys. Rev. Lett. **50**, 1293 (1983); M. Aono, R. Souda, C. Oshima, and Y. Ishizawa, Phys. Rev. Lett. **51**, 801 (1983).

[5] M. Aono and R. Souda, Jpn. J. Appl. Phys. **24**, 1249 (1985).

[6] R. Souda, M. Aono, C. Oshima, S. Otani, and Y. Ishizawa, Nucl. Instrum. Methods B **15**, 138 (1986).

[7] R. Souda, C. Oshima, S. Otani, Y. Ishizawa, and M. Aono, Surf. Sci. **199**, 154 (1988); M. Katayama, E. Nomura, N. Kanekama, H. Soejima, and M. Aono, Nucl. Instrum. Methods B **33**, 857 (1988).

[8] T. L. Porter, C. S. Chang, and I. S. T. Tsong, Phys. Rev. Lett. **60**, 1739 (1988).

[9] T. L. Porter, C. S. Chang, U. Knipping, and I. S. T. Tsong, Phys. Rev. B **36**, 9150 (1987).

[10] J. A. Yarmoff, D. M. Cyr, J. H. Huang, S. Kim, and R. S. Williams, Phys. Rev. B **33**, 3856 (1986).

[11] J. A. Yarmoff and R. S. Williams, J. Vac. Sci. Technol. A **4**, 1274 (1986); R. S. Williams and J. A. Yarmoff, Nucl. Instrum. Methods **218**, 235 (1983).

[12] J. H. Huang and R. S. Williams, Phys. Rev. B **38**, 4022 (1988); J. Vac. Sci. Technol. A **6**, 689 (1988).

[13] H. Niehus and G. Comsa, Surf. Sci. **140**, 18 (1984); **152/153**, 93 (1985); **151**, L171 (1985).

[14] H. Niehus, Surf. Sci. **145**, 407 (1984).

[15] H. Niehus and G. Comsa, Nucl. Instrum. Methods B **15**, 122 (1986).

[16] H. Niehus, J. Vac. Sci. Technol. **5**, 751 (1987).

[17] H. Niehus, K. Mann, B. N. Eldridge, and M. L. Yu, J. Vac. Sci. Technol. A **6**, 625 (1988).

[18] H. Niehus, C. Hiller, and G. Comsa, Surf. Sci. **173**, L599 (1986).

[19] J. Möller, H. Niehus, and W. Heiland, Surf. Sci. **166**, L111 (1986).

[20] L. Marchut, T. M. Buck, G. H. Wheatley, and C. J. McMahon, Jr., Surf. Sci. **141**, 549 (1984).

[21] T. M. Buck, I. Stensgaard, G. H. Wheatley, and L. Marchut, Nucl. Instrum. Methods **170**, 519 (1980).

[22] J. M. van Zoest, J. M. Fluit, T. J. Vink, and B. A. van Hassel, Surf. Sci. **182**, 179 (1987).

[23] J. W. Rabalais, J. A. Schultz, R. Kumar, and P. T. Murray, J. Chem. Phys. **78**, 5250 (1983).

[24] J. W. Rabalais, CRC Crit. Rev. Solid State Mater. Sci. **14**, 319 (1988); B. J. J. Koeleman, S. T. deZwart, A. L. Boers, B. Polsema, and L. K. Verheij, Phys. Rev. Lett. **56**, 1152 (1986); B. Visscher, Ph.D. dissertation, Rijksuniversiteit, Groningen, The Netherlands, 1988.

[25] D. P. Woodruff and T. A. Delchar, *Modern Techniques of Surface Science* (Cambridge University Press, Cambridge, 1986).

[26] E. A. Mashkova and V. A. Molchanov, *Medium Energy Ion Reflection From Solids* (North-Holland, Amsterdam, 1985).

[27] J. F. Zeigler, J. P. Biersack, and U. Littmark, *The Stopping and Range of Ions in Solids* (Pergamon, New York, 1985).

[28] J. W. Rabalais, J. N. Chen, R. Kumar, and M. Narayana, J. Chem. Phys. **83**, 6489 (1985); Chem. Phys. Lett. **120**, 406 (1985); J. W. Rabalais, J. N. Chen, and R. Kumar, Phys. Rev. Lett. **55**, 1124 (1985).

[29] U. Wille and R. Hippler, Phys. Rep. **132**, 129 (1986).

[30] H. D. Hagstrum, Phys. Rev. **96**, 336 (1954); H. D. Hagstrum, in *Electron and Ion Spectroscopy of Solids*, edited by L. Fiermans, J. Vennik, and W. Dekeyser (Plenum, New York, 1978).

[31] U. Fano and W. Lichten, Phys. Rev. Lett. **14**, 627 (1965); W. Lichten, J. Phys. Chem. **84**, 2102 (1980); M. Barat and W. Lichten, Phys. Rev. A **6**, 211 (1972).

[32] H. L. Davis and G.-C. Wang, Bull. Am. Phys. Soc. **29**, 221

(1984).
[33] J. B. Benziger and R. E. Preston, Surf. Sci. **151**, 183 (1985).
[34] G.-C. Wang, J. M. Pimbley, and T.-M. Lu, Phys. Rev. B **31**, 1950 (1985).
[35] J. F. Wendelken, J. Vac. Sci. Technol. A **6**, 662 (1988).
[36] W. P. Ellis and R. R. Rye, Surf. Sci. **161**, 278 (1985).
[37] H. Bu, O. Grizzi, M. Shi, and J. W. Rabalais, paper II, this issue, Phys. Rev. B **40**, 10 147 (1989).
[38] M. Shi, O. Grizzi, H. Bu, J. W. Rabalais, and R. R. Rye, paper III, this issue, Phys. Rev. B **40**, 10 163 (1989).
[39] O. Grizzi, M. Shi, H. Bu, and J. W. Rabalais, Rev. Sci. Instrum (to be published).
[40] J. W. Rabalais and J. N. Chen, J. Chem. Phys. **85**, 3615 (1986).
[41] J. N. Chen, M. Shi, and J. W. Rabalais, J. Chem. Phys. **86**, 2403 (1987).
[42] J. A. Schultz, Y. S. Jo, and J. W. Rabalais, Solid State Commun. **55**, 957 (1985).
[43] M. H. Mintz, J. A. Schultz, and J. W. Rabalais, Surf. Sci. **146**, 457 (1984); J. A. Schultz, M. H. Mintz, T. R. Schuler, and J. W. Rabalais, *ibid.* **146**, 438 (1984).
[44] P. Hochmann, M. Kilburn, M. Shi, and J. W. Rabalais (unpublished).
[45] J. M. MacLaren, J. B. Pendry, R. J. Rous, D. K. Saldin, G. A. Somorjai, M. A. Van Hove, and D. D. Vvedensky, *Surface Crystallgraphic Information Service* (Reidel, Dordrecht).
[46] S. R. Kasi, M. A. Kilburn, H. Kang, J. W. Rabalais, L. Tavernini, and P. Hochmann, J. Chem. Phys. **88**, 5902 (1988).
[47] R. S. Daley, J. H. Huang, and R. S. Williams (unpublished).
[48] O. P. Gupta and M. P. Hemkar, Z. Naturforsch. Teil A **32**, 1495 (1977); P. Debrunner and R. J. Morrison, Rev. Mod. Phys. **36**, 463 (1964).
[49] W. Eckstein, V. A. Mochanov, and H. Verbeek, Nucl. Instrum. Methods **149**, 599 (1978); H. Verbeek, W. Eckstein, and R. S. Bhattacharya, J. Appl. Phys. **51**, 1783 (1979).